MICHIGAN STATE
UNIVERSITY

National Superconducting Cyclotron Laboratory

TOTAL REACTION AND NEUTRON-REMOVAL CROSS SECTIONS OF 30A - 60A MeV He AND Li ISOTOPES ON Pb

R.E. WARNER, M.H. McKINNON, N.C. SHANER, F.D. BECCHETTI, A. NADASEN, D.A. ROBERTS, J.A. BROWN, A. GALONSKY, J.J. KOLATA, R.M. RONNINGEN, M. STEINER, and K. SUBOTIC

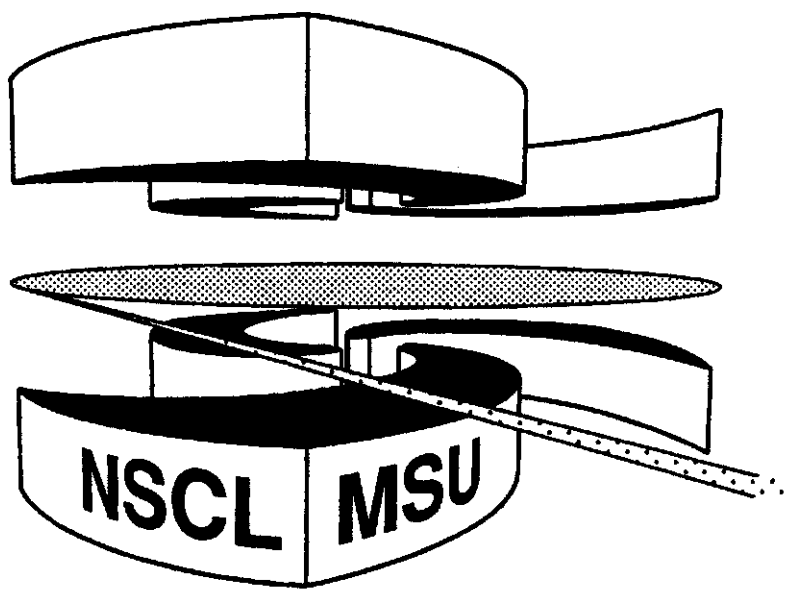

MSUCL-1159 **JUNE 2000**

Total reaction and neutron-removal cross sections of 30A-60A MeV He and Li Isotopes on Pb

R.E. Warner[1], M.H. McKinnon[1], N.C. Shaner[1], F.D. Becchetti[2], A. Nadasen[3], D.A. Roberts(*), J.A. Brown[4], A. Galonsky[5], J.J. Kolata[6], R.M. Ronningen[5], M. Steiner[5], and K. Subotic[7]

(1) Oberlin College, Oberlin, Ohio 44074

(2) University of Michigan, Ann Arbor, Michigan 48109

(3) University of Michigan, Dearborn, Michigan 48128

(4) Millikin University, Decatur, Illinois 62522

(5) National Superconducting Cyclotron Laboratory, East Lansing, Michigan 48824

(6) University of Notre Dame, Notre Dame, Indiana 46556

(7) Institute of Nuclear Sciences, VINCA, Belgrade 11001, Yugoslavia

ABSTRACT

Total reaction cross sections σ_R of 30A-60A MeV ^{4,6,8}He and ^{6,7,8,9,11}Li on Pb, and 2n-removal cross sections σ_{-2n} of ^{6,8}He and ^{11}Li on Pb, were measured by injecting magnetically separated, focused, monoenergetic, secondary beams of those projectiles into a telescope containing Pb targets separated by thin Si detectors. All these σ_R's (except ^{4}He), and σ_{-2n} for ^{6}He and ^{11}Li, are underpredicted by microscopic model calculations which include only nuclear forces. Better agreement is achieved by including electromagnetic dissociation in the model, for those projectiles for which either the electric dipole response functions or the dominant

photodissociation cross sections were known. The cross sections σ_{-4n} for ^{8}He, σ_{-xn} for ^{7,8,9}Li, and $(\sigma_{-3n}+\sigma_{-4n})$ for ^{11}Li were found to be $\leq$0.7 b. All σ_R's were measured to better than 5% accuracy, showing that the method is usable for other target elements sandwiched into a Si telescope.

PACS: 25.60.Dz, 24.10.-i

KEYWORDS: total reaction cross section; neutron-removal cross sections; 60A MeV radioactive nuclear beams (^{4,6,8}He and ^{6,7,8,9,11}Li); ^{nat}Pb target; microscopic model calculations; electromagnetic dissociation

I. INTRODUCTION

During the last decade we measured total reaction cross sections σ_R and one- or two-nucleon removal cross sections σ_{-xN} for many light projectiles (A=2 through 17) incident upon silicon detectors used as active targets. The projectiles included the 2n-halo nuclei ^{6}He and ^{11}Li [1] and the proton-halo candidates ^{8}B, ^{12}N, and ^{17}Ne [2], at energies up to about 60 MeV/nucleon. These measurements are intended to test nuclear models and get information about projectile matter distributions including, in some cases, their halo structure.

The best fits to our data were obtained from a microscopic (Glauber) model [3], though strong absorption and conventional optical model fits (where parameters were available) were also attempted. The microscopic model starts from known nucleon-nucleon interaction cross sections, σ_{NN}, and assumed matter distributions. It finds the reaction probability in an elementary volume where projectile and target overlap, and integrates this probability over the nuclear volumes, the trajectory, and all impact parameters. At energies below 100 MeV/nucleon the model is relatively insensitive to σ_{NN}; the latter is so large that, on orbits with impact parameters less than the strong interaction radius, reactions nearly always occur. Thus the model becomes particularly appropriate for testing nuclear matter distributions. While the model was first applied to high-energy data [3], it works surprisingly well even for energies of a few MeV/nucleon for Si targets [4], on which most reactions are caused by nuclear rather than Coulomb forces.

A remaining question is the model's utility at low and medium energies for heavy targets, for which electromagnetic dissociation (EMD) is a prominent effect. The existing σ_R and σ_{-xN} data for ^{11}Li+Pb at energies below 100 MeV/nucleon agree less well with the theory than do higher-energy data [5-9].

Therefore we have now measured σ_R and σ_{-xN} for most bound He and Li isotopes on Pb, at energies up to about 60 MeV/nucleon, and we compare them with model predictions.

In previous measurements [1,2], secondary beams of the projectiles of interest were injected into, and stopped in, a telescope containing only Si detectors. Total energy-deposit spectra were observed, and projectiles which had energy losses other than those expected from ionization alone were identified as reacting. Further, those with appropriate energy deficits (e.g., 2/11 of the incident energy for ^{11}Li) could be identified as 2n-removal reactions. The use of a series of Si detectors provided measurements in different projectile energy ranges, giving information about the energy dependence of σ_R and σ_{-xN}. In the present measurements, Pb targets were placed between the Si detectors in a telescope and the Si background, known from earlier measurements [1], was subtracted.

Section II of this paper describes the experimental procedure, including the identification of reactions. Unlike the earlier measurements, there are large unmeasured energy losses in the targets of interest, requiring new data analysis techniques. These are described in Section III, where we show how σ_R and σ_{-xN} are deduced from the reaction yields. Section IV presents microscopic model calculations, showing that the data are reasonably well fitted by this model only in those cases where we can include EMD effects. Section V contains our conclusions.

II. EXPERIMENTAL PROCEDURE

The projectiles were produced at the National Superconducting Cyclotron Laboratory by fragmentation of a primary 80A MeV ^{18}O beam, up to 50 pnA in intensity, incident upon a 0.75 gm/cm^2 Be target at the entrance to the A1200 analyzing system. An achromatic Al wedge, placed in an intermediate image plane, reduced their energy while preserving their momentum resolution. Finally, the system focussed the secondary beams on the telescope shown in Fig. 1. The energies for ^4He and ^6Li were chosen so that they stopped halfway through Detector 8; other beams stopped halfway through Detector 9.

As in the earlier work [1], anomalous signals from the Si detectors identified those projectiles of interest which underwent reactions. Unlike those earlier experiments, the intended targets were Pb sheets, 1.9 mm thick for the He beams and 1 mm thick for the Li beams, placed between detectors.

The first two (position-sensitive) detectors selected a beam of 6 mm radius; their energy-loss signals rejected beam contaminants. Detector 1 was about 60 cm upstream from Detector 2. The remaining components were close-packed, with Detector 9 about 17 cm from Detector 2.

The reactions were of two basic types, requiring separate identification methods. Those where the projectile changed its atomic number in a given detector ("Z-changing"), or in the preceding Pb target, generally gave anomalous pulses in that detector. However, neutron-removal reactions produced charged fragments which traversed one or two detectors before their signals could be distinguished from those of nonreacting projectiles.

Examples of fragment groups from n-removal reactions appear in Figures 2 and 3, which are event plots of energy loss in Detector 7 vs. the combined losses (E89) in Detectors 8 and 9. Detector energy calibrations were obtained from detector thicknesses and the ionizing powers [10] and pulse heights of

nonreacting projectiles. The fragments were identified using the algorithm

$$R = aE^p \qquad (1)$$

where R and E are the range and energy, and $p \approx 1.78$ empirically gave optimum resolution of particle groups.

Figure 2 shows an intense group of α-particles from ^{6}He dissociation. Nearly all nonreacting ^{6}He projectiles have $E_7 \approx 5.5$ MeV and $E_{89} \approx 140$ MeV, but there are three additional categories. Those below the main group, less than 1% of the total, have channeled in Detector 7; those to its right represent pileup. Energy-degraded ^{6}He's appear above and to the left; their number can be explained by energy straggling throughout the telescope but must include some inelastic scattering events. Events in the band marked ΔE_7 react in Detector 8 or 9 after avoiding reactions in preceding elements; we call these events the "normal-ΔE_7 band". Reaction products with Z = 1 appear near the origin. Many reactions (not shown), at the origin or on the vertical axis, have products which stop before or in Detector 7.

Figure 3, for incident ^{11}Li, shows similar features. The most intense reaction group, as expected, is ^{9}Li. Multineutron removal to ^{7,8}Li, as well as particle groups with Z=1 (near the origin) and Z=2 are observed. ^{11}Li, unlike ^{6}He, shows a resolved low-energy group of nonreacting projectiles, making up about 0.1% of the beam. We verified that their signals could not simulate reactions, but nevertheless we rejected these events during analysis. No other projectiles showed this apparent beam defect.

Energy spectra of identified ^{4}He from ^{6}He dissociation, and ^{9}Li from ^{11}Li dissociation, are shown in Figs. 4 and 5 respectively. In both cases, some fragments formed in the final Pb target entered detector 7 with ionizing powers similar to nonreacting projectiles, and were lost in the normal-ΔE_7 band. All events in this band were rejected by software gates; later we

estimate, and correct for, the number of rejected 2n-removal events which should be counted.

Other reaction events, mainly Z-changing except for some n-removal events occurring early in the telescope, were identified in the one-dimensional energy spectra of Detectors 3 through 7. For example, Fig. 6(a) shows the total event spectrum of Detector 7 for incident ^{9}Li, after rejection of n-removal and pileup events by software gates. The peak near 10 MeV, due to nonreacting projectiles, has a low-energy shoulder due to channeling in this detector. To obtain the reaction yield spectrum it was necessary to know the line shape from nonreacting ^{9}Li projectiles. Thus we first subtracted a spectrum of projectiles, known not to react, from the total spectrum. These nonreacting projectiles, including both those which channeled in Detector 7 and those which did not, had normal energy losses in Detector 8 and were identified as ^{9}Li in Detectors 7 through 9. Tight gates on these parameters rejected some nonreaction events with large energy straggling, causing the small subsidiary peaks in the difference spectrum.

Except in the channeling region, the non-reaction yield outside the vertical dashed lines of Fig. 6a is negligible. Further, the difference spectrum in the channeling region connects smoothly with the reaction yield at lower and higher energies. Thus all events in the difference spectrum outside the dashed lines were counted as reactions, as were the interpolated events (under the solid line) beneath the peak. The latter events typically make up 3-5% of the total reaction yield.

The events identified in spectra such as Fig. 6a were added to the n-removal events found by analyzing two-dimensional spectra, as described in Section III. The combined reaction probability η_7, for reactions occurring in Detector 7 and all detectors and lead targets which precede it, is the ratio

of the combined reaction yield to the incident flux. Section IIID shows how σ_R is found from η_7 and other data.

One concern was that elastically scattered projectiles might simulate reaction events by leaving the telescope, since Detectors 8 and 9 had smaller areas than the others. We observed outscattering in spectra of Detector 7, (where scattered projectiles have their maximum dE/dx) in anticoincidence with Detector 8. A typical result is shown in Fig. 6(b). The outscattered events, for ^{7}Li and all other projectiles, are inside the interpolation region and therefore cannot simulate reactions. The observed outscattering yield was 0.7% of the incident beam for ^{6}Li and less for other projectiles.

III. EXPERIMENTAL RESULTS

IIIA. 2n-removal from ^{11}Li

The 2n-removal yield from ^{11}Li included two contributions. Events from most of the telescope are identified <u>above</u> the normal-ΔE_7 band (see Fig. 3); their ΔE_7 spectrum is shown in Fig. 5a. Fig. 5b shows the $\Delta E_8+\Delta E_9$ energy spectrum for all events <u>in</u> the band. The peak near 220 MeV includes some 2n-removal events from the last Pb target, and a smaller number of 3n- and 4n-removal events. The deduced events in this peak lie above the solid interpolation line; dashed lines indicate the assigned uncertainty. After subtracting the 3n- and 4n-removal contributions (Section IIIC), the deduced 2n-yield makes up (24±5)% of the total 2n-removal yield. ^{11}Li+Si events, for which $\sigma_{-2n} \simeq 0.4$ barns [1], are about 5% of the observed 2n-removal yield and, after subtraction, contribute negligibly to the experimental error.

Events were lost if the ^{9}Li fragment itself reacted later, or stopped before Detector 8 due to its momentum transfer in the reaction. We estimated the detection efficiency by calculating the ΔE_7 spectrum using the σ_R for

^{9}Li+Pb measured in this experiment and σ_{-2n} obtained from Esbensen and Bertsch [11]. The fragment momentum distribution was assumed to be Lorentzian [12]

$$N(p)dp = \frac{2\,\Gamma\,p^2\,dp}{\pi\,(\Gamma^2/4 + p^2)^2} \qquad (2)$$

with isotropic emission in the ^{11}Li c.m. system. We took Γ to be 45 MeV/c [13] and found the fragment detection efficiency to be 0.94 ± 0.03.

Interpolation and fragment-loss uncertainties were combined in quadrature to obtain a σ_{-2n} of 4.4 ± 0.3 barns averaged over the projectile energies (27 to 55 MeV/nucleon) in all four Pb targets. Figure 7 shows this and other known data for 2n-removal from ^{11}Li.

Uncertainties in extrapolation to determine the late fragmentation yield (i.e., events in the ΔE_7 band) affect both our measured σ_{-xn} and σ_R data. Some fragments produced early in the telescope stop in Detector 7 and therefore are not identified. However they are correctly counted in σ_R since they give anomalous signals in one or more singles spectra including that of Detector 7.

IIIB. 2n-removal from ^{6}He and ^{8}He

In contrast to ^{11}Li→^{9}Li dissociation, only about half of the α-particles from ^{6}He dissociation reached Detectors 7 and 8 for identification, due to their larger relative mass difference and the thicker Pb targets. Therefore, to find σ_{-2n}, we compared the expected α-yield in the region between the normal-ΔE_7 band and detector saturation (i.e., E_α between 6 and 18 MeV) with the yield predicted by a calculation similar to that described above for ^{11}Li.

The basis of our σ_{-2n} prediction is described in Section IVA. A momentum distribution parameter, Γ = 120 MeV/c, has been reported [12,14] only for a C target at 0.4 GeV/nucleon. The distribution must be narrower at our energy,

since many forward-emitted fragments would not conserve energy if Γ = 120 MeV/c. We therefore used a renormalized distribution similar to Eq. (2), cut off at the largest momentum which conserved energy for those fragments. Fortunately the results are insensitive to Γ; when Γ was varied from 40 to 120 MeV/c the predicted yield varied by only 3%. The ratio of observed to predicted events was 0.97 ± 0.03, increasing to 1.05 ± 0.04 after correction for beam attenuation before dissociation and fragment reactions afterwards. We thus obtained σ_{-2n} = 1.46 ± 0.06 bn.

Figure 4a shows the observed ΔE_7 spectrum and the fit predicted with this calculation. Figure 4b shows the spectrum of incident energies at which ^{6}He dissociates, predicted for the events detected both in and above the ΔE_7 band. The mean dissociation energy for these events is 37 MeV/nucleon, with 80% of them lying between 28 and 52 MeV/nucleon.

For the ^{8}He→^{6}He analysis we again varied Γ from 40 to 120 MeV/c, since the fragment momentum distributions from ^{8}He and ^{6}He on light targets at high energies [15,16] are similar. One source of uncertainty is that we have no predictions for σ_{-2n} vs. energy which include EMD. We analyzed the data assuming (a) no energy dependence and (b) the same dependence as for ^{6}He. The latter seems more realistic since the energy dependence in the microscopic model is mainly that of the nucleon-nucleon cross section. Our result, σ_{-2n} = 0.89 ± 0.08 barns, is consistent with both analyses; 80% of the events occur for incident energies between 26 and 45 MeV/nucleon.

IIIC. Other neutron-removal reactions

We give only an estimate of σ_{-4n} for ^{8}He→^{4}He +4n, since the ^{4}He have only a short range in the Pb targets and their momentum distributions are unknown. If we assume that the charged fragments are spectators (i.e., no momentum is transferred to them in the reaction), then all ^{6}He's produced in the last two

Pb targets are identified in Detectors 7 through 9 while α-particles are collected from only the last 1.5 mm of the last target. From the ratios of the identified yields and of the target thicknesses contributing to those yields, we found $\sigma_{-4n} \approx 0.5$ barns. The 4n-removal cross section for ^{8}He+Si was also found, earlier, to be about half that for 2n-removal [1]; that result too was approximate since it was found by decomposing the n-removal peak in the total energy spectrum.

Other n-removal cross sections are approximate, for similar reasons. All spectator ^{8}Li fragments produced from ^{11}Li in the four Pb targets, and about 70% of the spectator ^{7}Li fragments, are identifiable. Their observed yield contributes 0.55 barn to σ_R, leading to a combined cross section of about 0.7 barn for removing 3 or 4 neutrons from ^{11}Li. Similarly, the summed n-removal cross sections from both ^{8}Li and ^{9}Li are about 0.6 barns and that from ^{7}Li is about 0.1 barn.

IIID. Energy-averaged total reaction cross sections.

The probability η_3 of a reaction occuring in any of the first 3 Si detectors is given by

$$1-\eta_3 = \exp\,(-\sigma_{R,Si} n_{Si}) \qquad (3)$$

where $\sigma_{R,Si}$ is the energy-averaged total reaction cross section on Si and n_{Si} is the total nuclei per unit area in those detectors. Likewise η_7, the probability of a reaction in or before Detector 7 is given by

$$1-\eta_7 = \exp\,(-\sigma_{R,Pb} n_{Pb} + \sigma_{R,Si} n_{Si}) \qquad (4)$$

where the exponential arguments include contributions from all Pb targets and the first 7 detectors. Thus the total cross section on Pb, $\sigma_{R,Pb}$, energy-averaged over all 4 targets, is

$$\sigma_{R,Pb}\, n_{Pb} = \ell n\, [(1-\eta_3)/(1-\eta_7)] \;-\; \sigma_{R,Si}\, n_{Si}. \qquad (5)$$

where $\sigma_{R,Si}\, n_{Si}$ refers to only Detectors 4 through 7. Values of $\sigma_{R,Pb}$ obtained for all projectiles are given in Table I and shown in Figs. 8 and 9. The uncertainty in n_{Pb} due to target nonuniformity was ± 2%; that for n_{Si} was negligible.

$\sigma_{R,Si}$ was found by microscopic model calculations. The calculated $\sigma_{R,Si}$'s for all projectiles are plotted vs. energy in Figs. 3 through 5 of [Ref. 1]. Predicted rather than measured values were used in Eq. (5), since the original Si data of Ref. [1] are at slightly different energies. Since these data could be fitted to an accuracy of ±10% by these calculations, we assigned 10% uncertainty to $\sigma_{R,Si}$ in Eq. (5).

η_7 was found by adding the probability for n-removal reactions identified in Detectors 7 through 9 to that for other reactions observed in the singles energy spectrum of Detector 7. The uncertainty in the singles yield was taken to be 1/3 of the interpolated counts (see Fig. 6); that for the n-removal reactions included error estimates for setting identification gates and interpolating into the normal-ΔE_7-bands. This gave a typical uncertainty of ±3% in the logarithmic term of Eq. (3) and was the largest source of experimental uncertainty.

η_3, found by microscopic calculations, was also generally consistent with the η_3 measured from this detector's singles spectrum. The uncertainty, taken to be the difference between measurement and calculation, was included in our error analysis but was always less than that in η_7. Measurements of η_2, the reaction probability in Detector 2, also were consistent with microscopic calculations.

One uncorrected experimental error is our loss of inelastic scattering events to low-lying states in Pb, with the projectile remaining in its ground state. The group to the first excited state is generally the most prominent

[17,18]. Integration of the inelastic angular distribution for 60A MeV α-particles to this state in ^{208}Pb [19] gives a cross section of about 0.02 b. Similar values for 35A MeV ^{6}Li on ^{12}C, ^{28}Si, and ^{58}Ni [18] are about 0.03 b with little dependence on the target A. These cross sections are smaller than our stated uncertainties in σ_R. Alternately, our data may be considered measurements of the interaction cross section σ_I, which includes all events in which A and/or Z of the projectile changes.

Uncertainties due to counting statistics were negligible.

IIIE. σ_R(E) for ^{4}He and ^{6,7}Li

Total reaction cross sections for these three isotopes, which have very small n-removal cross sections, were found for the projectile energy ranges in individual Pb sheets by a method similar to that of the last subsection. For example, η_7 in Eq. (3) was replaced by η_4 to find σ_R for the first Pb target. The results, shown in Fig. 10, have larger uncertainties than the 4-target averages since the η's in consecutive detectors have smaller differences. The results for α+Pb are in excellent agreement with those of Auce et al. [20] at the energies where the data sets overlap. The lowest-energy ^{6}Li datum agrees with the optical-model prediction of Nadasen et al. [21], which was obtained from precision measurements of large-angle elastic scattering.

We report only the 4-target average σ_R's for other projectiles, since their n-removal cross sections are larger and of unknown energy dependence. Nevertheless these averages seem adequate for testing theoretical models, since the data of Fig. 10 and the microscopic calculations for all isotopes show only a weak energy dependence for σ_R at these energies.

IV. MICROSCOPIC MODEL PREDICTIONS

Previous measurements [1,2] on Si targets were analyzed in the context of a microscopic model which relates nuclear matter distributions and nucleon-nucleon interaction cross sections to σ_R and σ_{-2n} data. Therefore, for comparison, we interpret the present Pb data through similar calculations.

IVA. Predictions of σ_{-2n}

σ_{-2n} for ^{6}He+Pb was calculated as before [22] except that we avoid using an arbitrary cutoff radius for EMD. The probability $\chi_{val}(b)$ that the valence neutrons are not removed by the nuclear force, when the impact parameter is b, is

$$\chi_{val}(b) = \exp\left[-\sigma_{NN} \int ds \int\int\int \rho_{val}\, \rho_t\, dV_t\right]. \qquad (6)$$

The valence neutron and target matter densities in target volume dV_t are ρ_{val} and ρ_t. The nucleon-nucleon total cross section σ_{NN} is obtained from the Charagi-Gupta prescription [23], and ds is an element of the trajectory. The core survival probability χ_{core} is found by replacing ρ_{val} with ρ_{core} in Eq. (6). The ^{6}He densities ρ_{core} and ρ_{val} were taken to be two-term harmonic oscillator form factors [24], and ρ_t for Pb was a two-parameter Fermi (2pF) function [25]. The probability $P_{nuc}(b)$ that nuclear forces remove the valence neutrons at impact parameter b without disrupting the core is then

$$P_{nuc}(b) = \chi_{core}(b)\,[1 - \chi_{val}(b)] \qquad (7)$$

The probability of EMD when nuclear forces affect neither core nor valence nucleons is:

$$P_{coul}(b) = \chi_{core}(b)\,\chi_{val}(b)\,(16\pi^3/9\hbar c) \int N(\epsilon_1;E,b)\,[dB(\epsilon_1;E)/dE]\,dE \qquad (8)$$

where the electric dipole response function $dB(\epsilon_1;E)/dE$ [26] and the virtual photon density $N(\epsilon_1;E,b)$ [22] are integrated over all ^{6}He continuum energies. Finally we have

$$\sigma_{-2n} = 2\pi \int [P_{nuc}(b) + P_{coul}(b)]\, b\, db \qquad (9)$$

Our prediction for σ_{-2n} vs. energy appears in Fig. 4b. The predicted cross section, averaged over the distribution shown, is 1.39 b, in agreement with our measurement of 1.46 ± 0.06 b. The Coulomb cross section, i.e., the second term in Eq. (7), accounts for 60% of σ_{-2n}. In this decomposition, the nuclear cross section would equal σ_{-2n} if Coulomb forces were "turned off". To further test the method, we calculated σ_{-2n} for ^{6}He+Pb at 800A MeV to be 0.79 b, in agreement with the measurement of 0.85 ± 0.05 b [27].

The predictions of both σ_{-2n} and σ_R for ^{11}Li, shown in Fig. 7, are by H. Esbensen from a microscopic model [11] which includes the effect of spatial correlation between the two valence neutrons.

IVB. Predictions of σ_R

We first included only nuclear interactions in microscopic calculations of σ_R for all projectiles, as in Ref. [1], with projectile densities taken from Ref. [1]. The results (Table I) are too low for nearly all projectiles; that for ^{11}Li is too low by a factor of 2. This conclusively demonstrates the need to include EMD effects for all projectiles except ^{4}He, which was shown [28] to have an EMD cross section of less than 1% of σ_R. The previously-cited 2pF form factor [25] was used for the Pb target density. When instead the Pb density-functional form factors of Fayans et al. [29] were used, the predictions changed by less than 1%.

Table I shows that similar calculations agree with σ_R measurements for ^{8,9}Li + Pb at slightly higher energies [7], within the larger uncertainties of those data.

Strong absorption (SA) calculations using the formulae of Shen et al. [30] gave σ_R's 25% lower for ^{11}Li, and 5 to 10% lower for other projectiles, than the microscopic calculations; thus, they underpredict the ^{11}Li measurement by about 60%. Somewhat better SA results were obtained for the

same projectiles on Si [1]. For the Pb target we cannot expect good fits since the SA model does not explicitly include EMD.

Microscopic predictions including EMD effects are given in Table I for projectiles whose photodissociation cross sections or electric dipole response functions are known. For ^{6}He, in analogy to Eq. (7),

$$\sigma_R = 2\pi \int [1 - \chi_{val(b)}\chi_{core}(b) + P_{coul}(b)]\, b\, db \qquad (10)$$

Measured photodisintegration cross sections were used to include EMD for ^{6}Li and ^{7}Li, as described for ^{4}He in Ref. [29]. Since the virtual photon density falls rapidly with increasing E_γ, only photodissociation reactions which are prolific near the lowest threshold were needed; these are (γ,xn) for both ^{6,7}Li [31] and (γ,t) for ^{7}Li [32]. H. Esbensen [11] provided the σ_R for ^{11}Li.

The measured σ_R is at least as large for ^{6}He as for ^{8}He. One explanation is that σ_{-2n} is at least 50% larger for ^{6}He, and 60% of the ^{6}He σ_{-2n} comes from EMD, which must be larger for ^{6}He since the last 2 neutrons are less tightly bound.

An intuitively appealing subtraction relationship for 2n-halo nuclei, e.g.

$$\sigma_{-2n}(^{11}\text{Li}) = \sigma_R(^{11}\text{Li}) - \sigma_R(^9\text{Li}), \qquad (11)$$

was proposed by Ogawa et al. [33] and found to agree with high energy data. The equality holds when reactions of the halo nucleus include only core reactions and 2n-removal. The σ_R data of Table I yield 4.83 ± 0.37 b for the right-hand side of Eq. (11), agreeing with our measurement $\sigma_{-2n}(^{11}\text{Li}) = 4.4 \pm 0.3$ b. However, the ^{9}Li and ^{11}Li cross sections are measured for slightly different energy ranges. We therefore adjusted the ^{9}Li σ_R by assuming that its energy dependence follows the microscopic prediction; Eq. (9) then yields $\sigma_{-2n} = 4.81 \pm 0.37$ b. For ^{6}He, we predict $\sigma_{-2n} = 1.82 \pm 0.13$ b from the original data and 1.86 ± 0.13 b with the energy adjustment, exceeding our

measurement of 1.46 ± 0.06 b by more than 2 standard deviations. The discrepancy may result from motion of the ^{4}He core relative to the ^{6}He c.m., caused by the Fermi motion of the valence neutrons [34]. This would increase the effective size of the core and, therefore, the σ_R of ^{6}He. This effect is larger for ^{6}He than for ^{11}Li, owing to the greater mass and smaller binding energy of ^{11}Li.

V. CONCLUSIONS

Measurement of σ_R by placing Pb target foils between thin Si detectors seems capable of 5% accuracy, and therefore can generate data adequate for testing theoretical models. The success of the method shows that Si telescope measurements of σ_R for other solid targets are also feasible. Therefore, measurements on intermediate-mass targets would now be useful for testing the Z-dependence of EMD cross sections, which is model-dependent [9]. Studies on light targets (Be or C) would give more sensitive measurements of the projectile rms radii. A further justification for σ_R measurements at energies below 60 MeV/nucleon is that the large nucleon-nucleon interaction cross section at these energies increases the sensitivity of σ_R to the matter density in the halo region [2].

We offer the following suggestions for related theoretical studies. Electric dipole response functions for ^{8}He, ^{8}Li, and ^{9}Li are needed to resolve the discrepancies between measured and predicted microscopic σ_R's for these nuclei. Al Khalili et al. [35] showed that microscopic calculations using static densities underestimate the radii of halo nuclei, and three-body correlations must be included for a correct treatment. Their method was applied to the high energy data; an adaptation to our energies would now be of interest. Finally, microscopic calculations in which nucleon-target optical potentials replace nucleon-nucleon cross sections, as performed by Hencken et

al. [36] for the fragment momentum distributions from ^{8}B and ^{11}Be, would be welcome.

ACKNOWLEDGEMENTS

We thank Henning Esbensen, Sergei Fayans, Peter Schwandt, Ian Thompson, and Dave Youngblood for their advice and interest, and for sending us results of their calculations and measurements. We also thank Mu-Young Lee, Tom O'Donnell, K.A.G. Rao, Dan Sisan, and Bill Yuhasz for their help in setting up and running the experiment. The Howard Hughes Medical Institute and the McGregor-Oresman Fund supported the work of Megan McKinnon and Nathan Shaner. The work was also supported by the National Science Foundation under grants PHY-9722604 and -9804869 (UM-Ann Arbor), PHY-9602869 (UM-Dearborn), PHY-9528844 (NSCL), PHY-9401761 (Notre Dame), and PHY-9423659 (Oberlin).

REFERENCES

1. R.E. Warner et al., Phys. Rev. C 54, 1700 (1996); and references therein.

2. R.E. Warner et al., Phys. Rev. C 52, R1166 (1995); R.E. Warner et al., Nucl. Phys. A635, 292 (1998).

3. G.F. Bertsch, B.A. Brown, and H. Sagawa, Phys. Rev. C 39, 1154 (1989).

4. R.E. Warner and G.N. Felder, Phys. Rev. C 42, 2252 (1990).

5. D. Sackett et al., Phys. Rev. C 48, 118 (1993).

6. S. Shimoura, in Proceedings of the International Symposisum on Structure and Reactions of Unstable Nuclei, Niigata, Japan 1991, edited by K. Ikeda and Y. Suzuki (World Scientific, Singapore 1991), p. 132

7. B. Blank et al., Nucl. Phys. A555, 408 (1993); Z. Phys. A 340, 41 (1991).

8. F. Humbert et al., Phys. Lett. B 347, 198 (1995).

9. T. Kobayashi et al., Phys. Lett. B 232, 51 (1989).

10. Computer code TRIM, version 91.14, J.P. Biersack and J.F. Ziegler (1992).

11. H. Esbensen and G.F. Bertsch, Phys. Rev. C 46, 1552 (1992); and H. Esbensen, private communication.

12. P.G. Hansen, A.S. Jensen, and B. Jonson, Ann. Rev. Nucl. Part. Sci. 45, 591 (1995).

13. K. Riisager, in Proceedings of the Third International Conference on Radioactive Nuclear Beams, East Lansing, USA 1993, edited by D.J. Morrissey, (Editions Frontieres) p. 285

14. T. Kobayashi, Nucl. Phys. A538, 343c, (1992)

15. T. Kobayashi, O. Yamakawa, K. Omata, K. Sugimoto, T. Shimoda, N. Takahashi, and I. Tanihata, Phys. Rev. Letters 60, 2599 (1988)

16. T. Nilsson et al., Nucl. Phys. A598, 418 (1996)

17. J. Alster, Phys. Lett. B25, 459 (1967); Phys. Rev. 141, 1138 (1966).

18. A. Nadasen, M. McMaster, M. Fingal, J. Tavormina, J.S. Winfield, R.M. Ronningen, P. Schwandt, F.D. Becchetti, J.W. Jänecke, and R.E. Warner, Phys. Rev. C 40, 1237 (1989).

19. D.H. Youngblood, private communication.

20. A. Auce et al., Nucl. Phys. A, to be published

21. A. Nadasen, M. McMaster, M. Fingal, J. Tavormina, P. Schwandt, J.S. Winfield, M.F. Mohar, F.D. Becchetti, J.W. Jänecke, and R.E. Warner, Phys. Rev. C 39, 536 (1989).

22. R.E. Warner, Phys. Rev. C 55, 298 (1997).

23. S.K. Charagi and S.K. Gupta, Phys. Rev. C 41, 1610 (1990).

24. I. Tanihata, D. Hirata, T. Kobayashi, S. Shimoura, K. Sugimoto, and H. Toki, Phys. Lett. B 289, 261 (1992).

25. C.W. de Jager, H. de Vries, and C. de Vries, At. Data Nucl. Data Tables 14, 479 (1974).

26. B.V. Danilin, I.J. Thompson, M.V. Zhukov, and J.S. Vaagen, Nucl. Phys. A632, 383 (1998); and I.J. Thompson, private communication

27. I. Tanihata, Nucl. Phys. A522, 275c (1991).

28. R.E. Warner, M.H. McKinnon, H. Thirumurthy, and A. Nadasen, Phys. Rev. C 59, 1215 (1999)

29. S.A. Fayans, E.L. Trykov and D. Zawischa, Nucl. Phys. A568, 523 (1994); and S. Fayans, private communication.

30. W.-Q. Shen, B. Wang, J. Feng, W.-L. Zhan, Y.-T. Zhu, and E.-P. Feng, Nucl. Phys. A491, 130 (1989)

31. S.S. Dietrich and B.L. Berman, At. Data Nucl. Data Tables 38, 199 (1988)

32. D.M. Skopic, J. Asai, E.L. Tomusiak, and J.J. Murphy II, Phys. Rev. C 20, 2025 (1979).

33. Y. Ogawa, K. Kabana, and Y. Suzuki, Nucl. Phys. A543, 722 (1992)

34. J.A. Tostevin, J.S. Al-Khalili, M. Zahar, M. Belbot, J.J. Kolata, K. Lamkin, D.J. Morrissey, B.M. Sherrill, M. Lewitowicz, and A.H. Wuosmaa, Phys. Rev. C 56, R2929, (1997)

35. J.S. Al-Khalili, J.A. Tostevin, and I.J. Thompson, Phys. Rev. C 54, 1843 (1996)

36. K. Hencken, G.F. Bertsch, and H. Esbensen, Phys. Rev. C 54, 3043 (1996)

Table I. Measurements and microscopic predictions (in barns) of σ_R and σ_{-2n} for He and Li isotopes on Pb.

Type	Energy	Measurement	Predictions		Source
			no EMD	with EMD	
	(MeV/u)	(b)	(b)	(b)	
^{4}He, σ_R	35 to 73	2.69 ± 0.08	2.56	2.57	this work
^{6}He, σ_R	23 to 63	4.51 ± 0.10	3.33	4.06	this work
^{8}He, σ_R	19 to 53	4.38 ± 0.11	3.62		this work
^{6}Li, σ_R	33 to 66	3.67 ± 0.14	3.28	3.56	this work
^{7}Li, σ_R	30 to 68	3.67 ± 0.12	3.19	3.80	this work
^{8}Li, σ_R	30 to 64	3.95 ± 0.14	3.29		this work
^{8}Li, σ_R	72 to 90	3.01 ± 1.85	3.17		Ref. [7]
^{9}Li, σ_R	29 to 60	3.87 ± 0.14	3.46		this work
^{9}Li, σ_R	66 to 95	3.69 ± 0.43	3.29		Ref. [7]
^{11}Li, σ_R	27 to 55	8.70 ± 0.34	4.72	7.96	this work
^{6}He, σ_{-2n}	28 to 52	1.46 ± 0.06	0.56	1.39	this work
^{8}He, σ_{-2n}	26 to 45	0.89 ± 0.08			this work
^{11}Li, σ_{-2n}	27 to 55	4.4 ± 0.3	1.4	3.95	this work

FIGURE CAPTIONS

1. Si detector and Pb target telescope (not to scale) used in this experiment.

2. Two-dimensional particle spectra from the last three detectors, with 64 MeV/nucleon ^{6}He incident upon the telescope shown in Fig. 1.

3. Similar to Fig. 2, for 56 MeV/nucleon incident ^{11}Li.

4. (a) Spectrum in Detector 7 of identified ^{4}He with energies above the ΔE_7 band (see Fig. 2), from incident ^{6}He. The histogram shows the model predictions described in text. (b) Model predictions of σ_{-2n}, and spectrum of energies at which ^{6}He's dissociate producing the fragments detected in this experiment.

5. (a) Similar to Fig. 4a, for ^{9}Li fragments from ^{11}Li. (b) Summed energies in last two detectors for events in the ΔE_7 band (Fig. 3) showing enhancement due to neutron-removal. Solid and dashed lines show deduced n-removal yield and its uncertainty.

6. (a) Energy-loss spectra of Detector 7 with incident ^{9}Li projectiles for all events, nonreaction events, and their difference interpolated to find reaction yield under the nonreaction peak. The ~10^4 events in a channel near zero energy are from reactions all of whose charged products stopped before Detector 7. (b) Spectra for incident ^{7}Li of all Detector 7 events, and of those in anticoincidence with Detector 8, showing signal due to events scattering out of Detector 8.

7. σ_R and σ_{-2n} for ^{11}Li+Pb vs. energy. Filled data points are from this experiment and open data points are from Refs. [5-9]. Curves show microscopic calculations by Esbensen [11].

8. Measured σ_R (filled data points) and σ_{-2n} (open data points) vs. A for He isotopes on Pb, with microscopic predictions including Coulomb dissociation (solid horizontal lines) and neglecting it (dashed lines). The two σ_R predictions for ^{4}He are indistinguishable. Data are averaged over energy ranges given in Table I.

9. Measured σ_R vs. A for Li isotopes on Pb, with microscopic predictions including Coulomb dissociation (solid horizontal lines) and neglecting it (dashed lines). Data are averaged over energy ranges given in Table I.

10. Measured σ_R vs. energy (filled data points) for ^{4}He, ^{6}Li, and ^{7}Li on Pb. Solid (dashed) curves show microscopic predictions including (neglecting) Coulomb dissociation. The diamond shows an optical model prediction of Ref. [21] for ^{6}Li, and open data points show ^{4}He +Pb data from Ref. [20]. Note the zero offsets of the vertical scales.

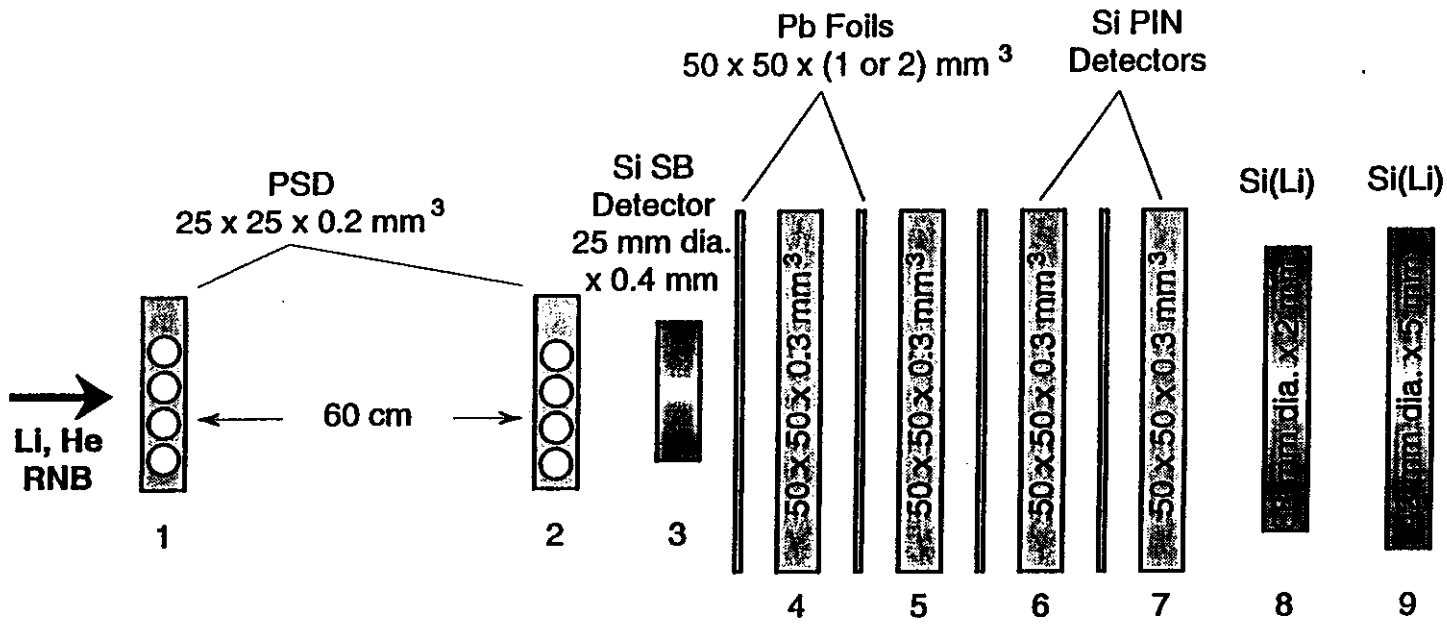
Pb Foils
50 x 50 x (1 or 2) mm 3
Si PIN
Detectors
PSD
25 x 25 x 0.2 mm 3
Si SB
Detector
25 mm dia.
x 0.4 mm
Si(Li)
Si(Li)
Li, He
RNB
60 cm
50x50x0.3mm3
50x50x0.3mm3
50x50x0.3mm3
50x50x0.3mm3
1
2
3
4
5
6
7
8
9

arner

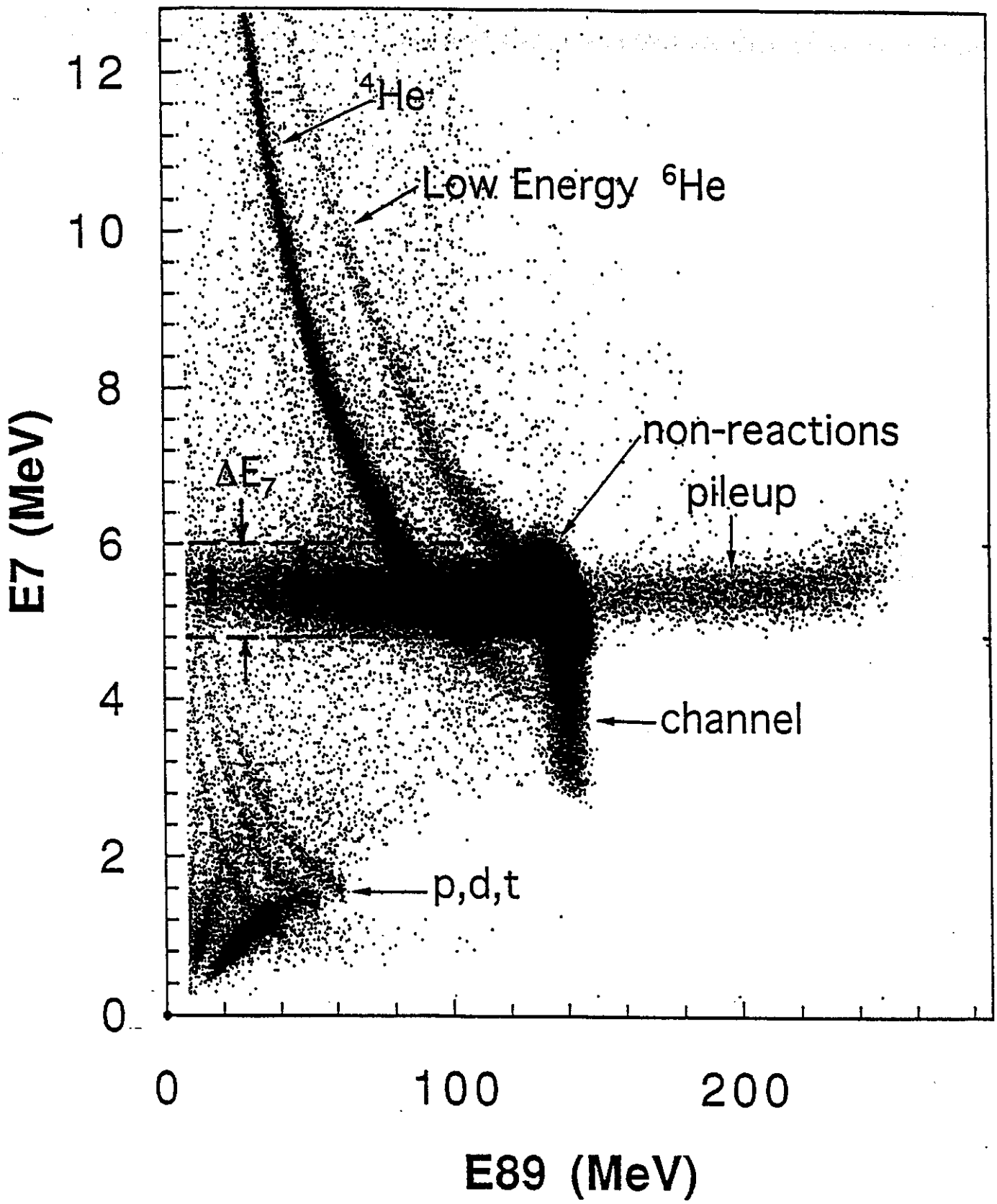
12
10
8
6
4
2
0
E7 (MeV)
0
100
200
E89 (MeV)
^{4}He
Low Energy ^{6}He
non-reactions
pileup
ΔE_7
channel
p,d,t

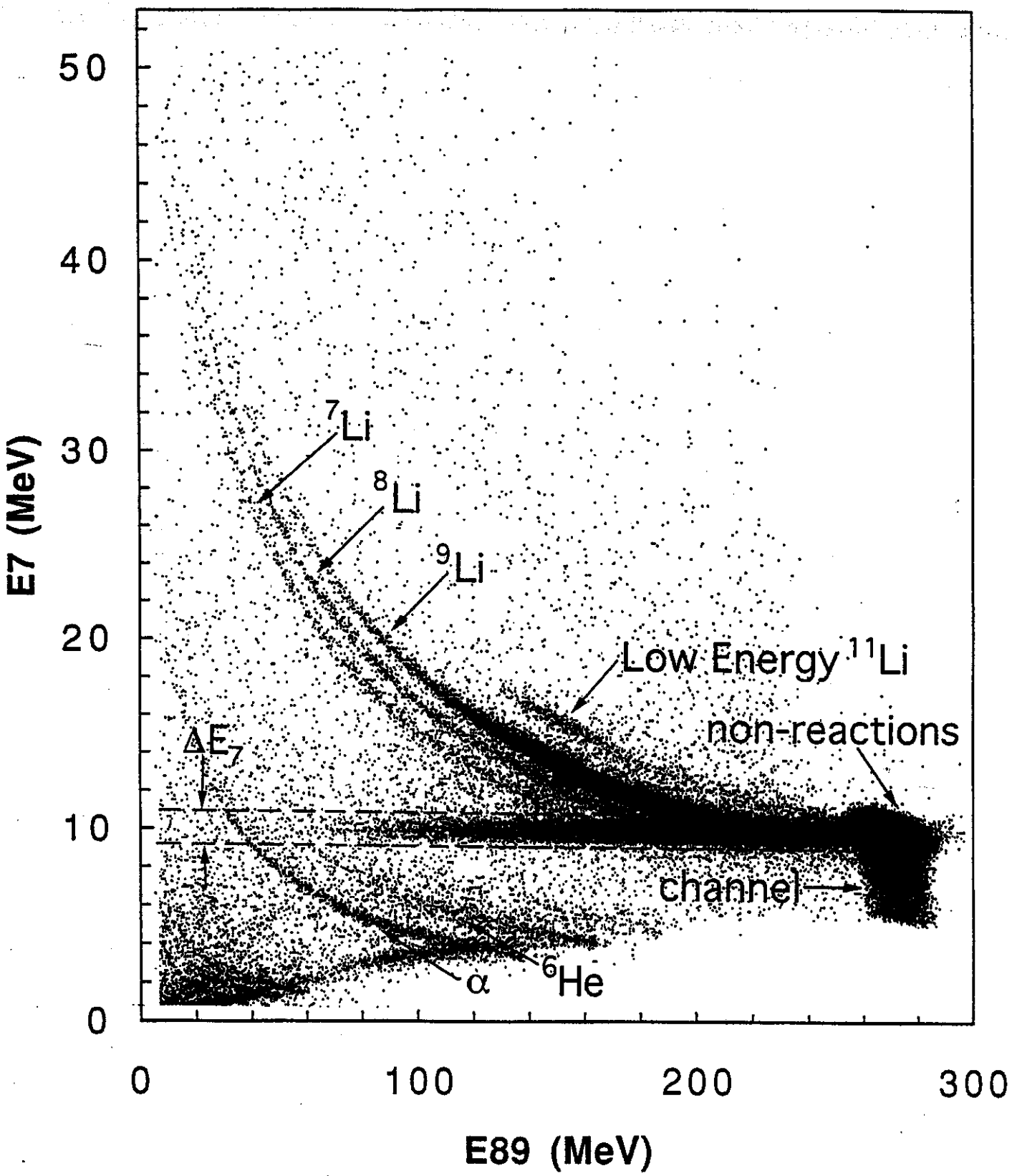

Warner
NEW Fig 3

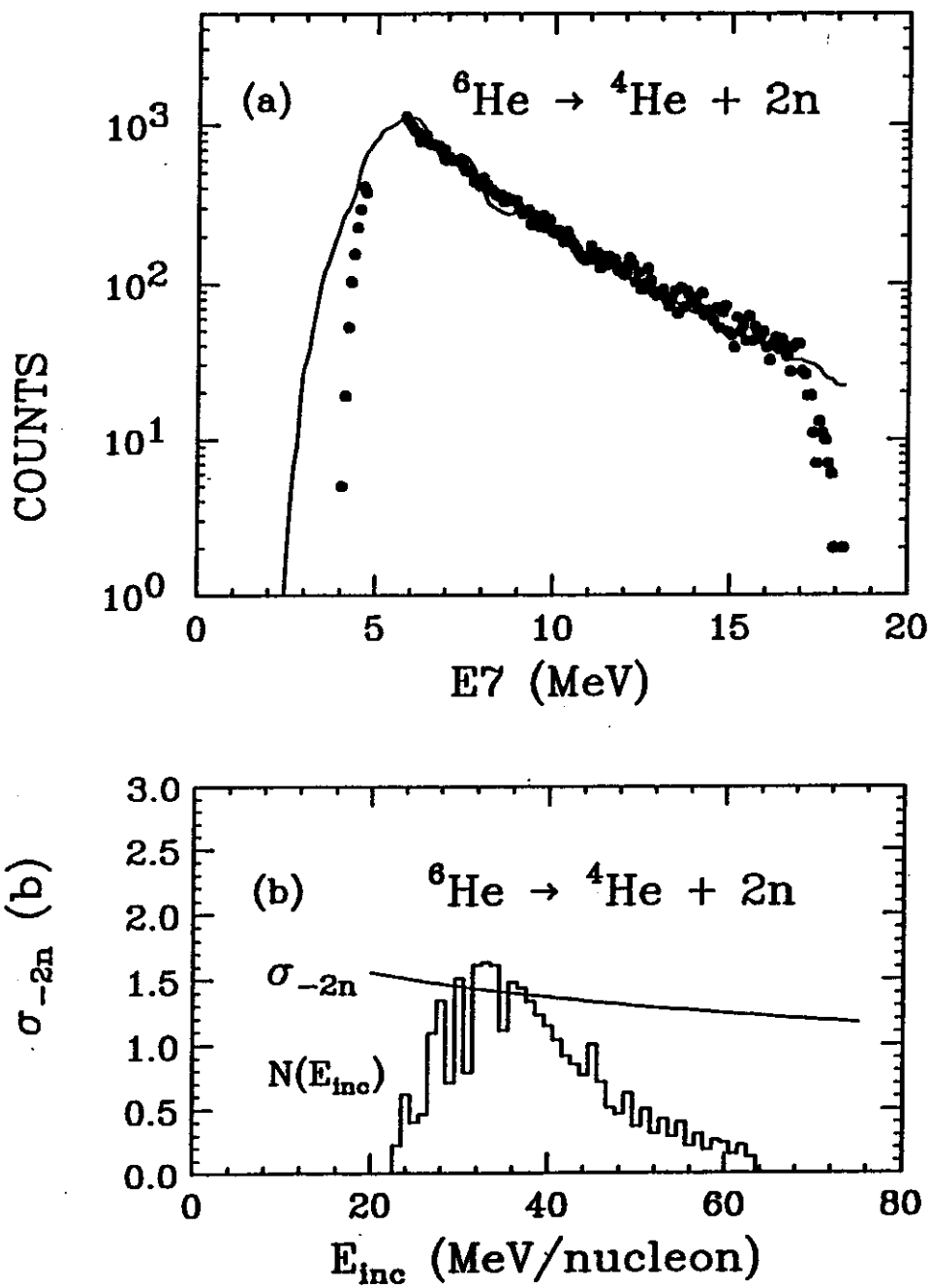
(a)
^{6}He → ^{4}He + 2n
COUNTS
10^3
10^2
10^1
10^0
0
5
10
15
20
E7 (MeV)
(b)
^{6}He → ^{4}He + 2n
σ_{-2n}
N(E_{inc})
σ_{-2n} (b)
3.0
2.5
2.0
1.5
1.0
0.5
0.0
0
20
40
60
80
E_{inc} (MeV/nucleon)

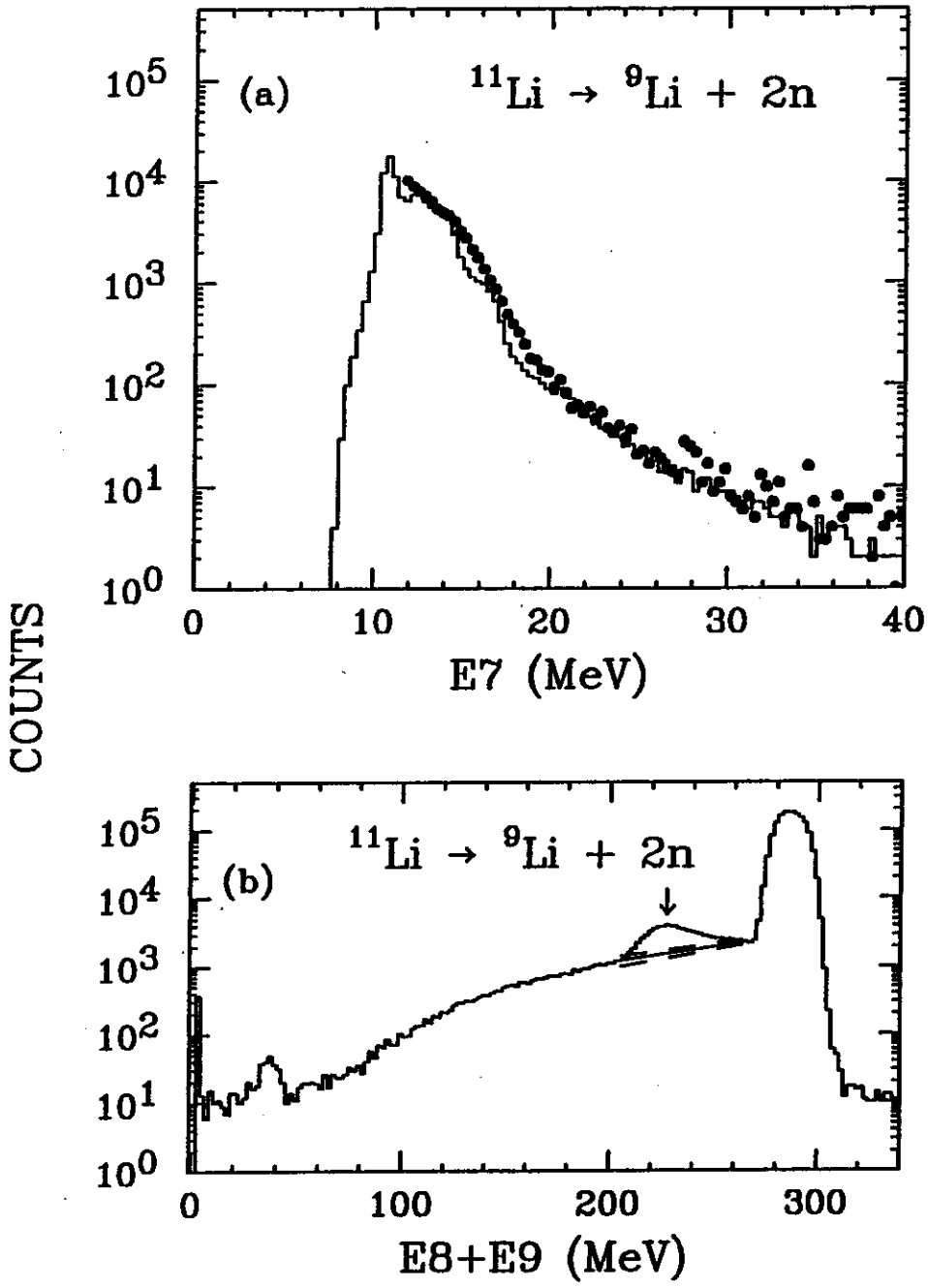

Warren
Fig. 5

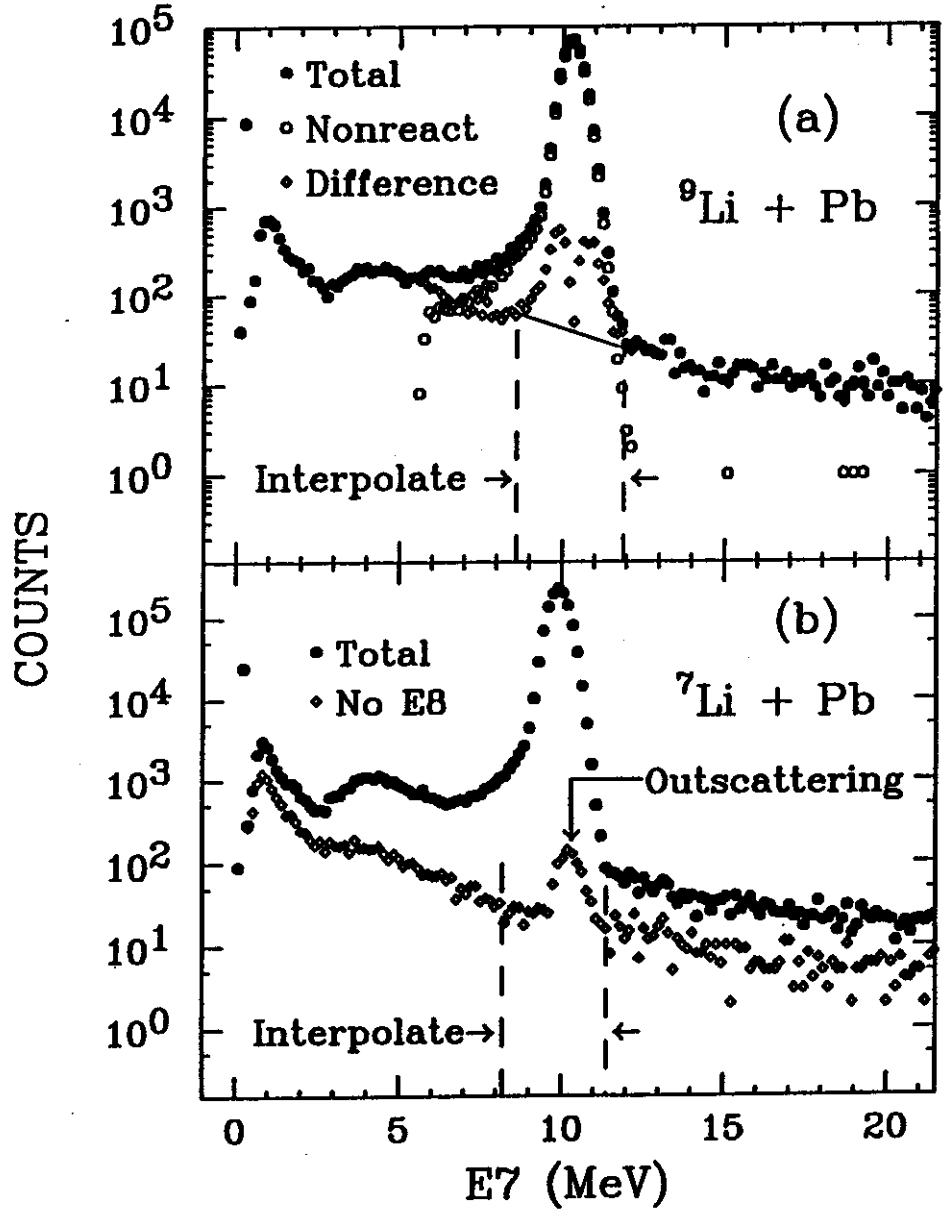
COUNTS
Total
Nonreact
Difference
(a)
^{9}Li + Pb
Interpolate →
Total
No E8
(b)
^{7}Li + Pb
Outscattering
Interpolate→
E7 (MeV)

Gunner Fig. 6

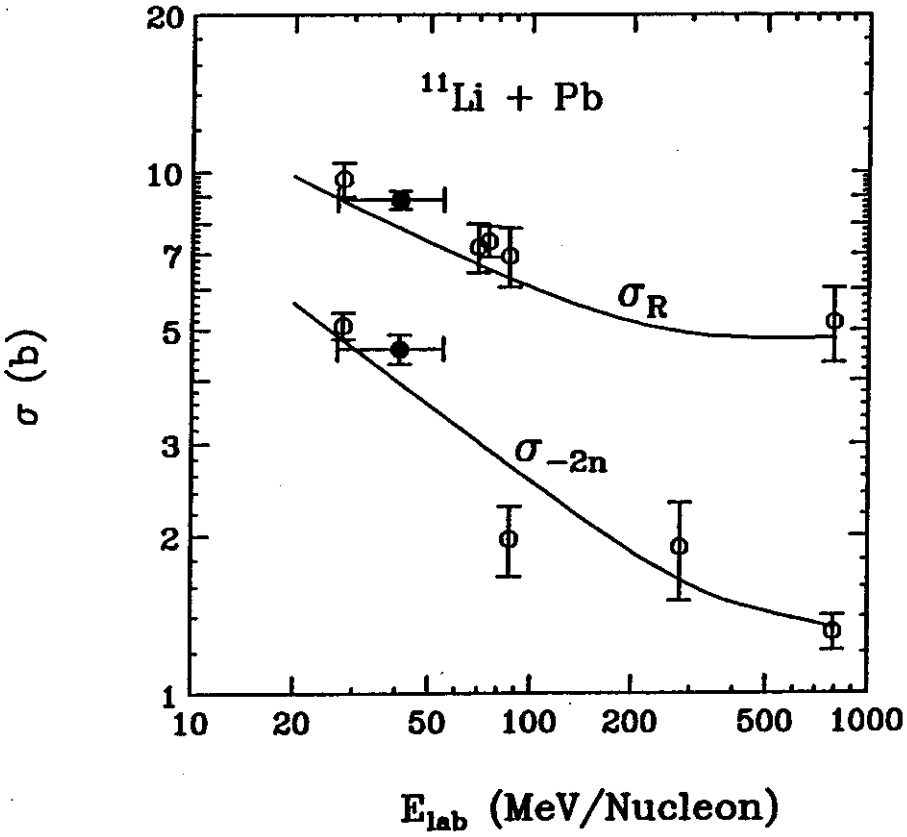
^{11}Li + Pb
σ_R
σ_{-2n}
σ (b)
E_{lab} (MeV/Nucleon)
20
10
7
5
3
2
1
10
20
50
100
200
500
1000

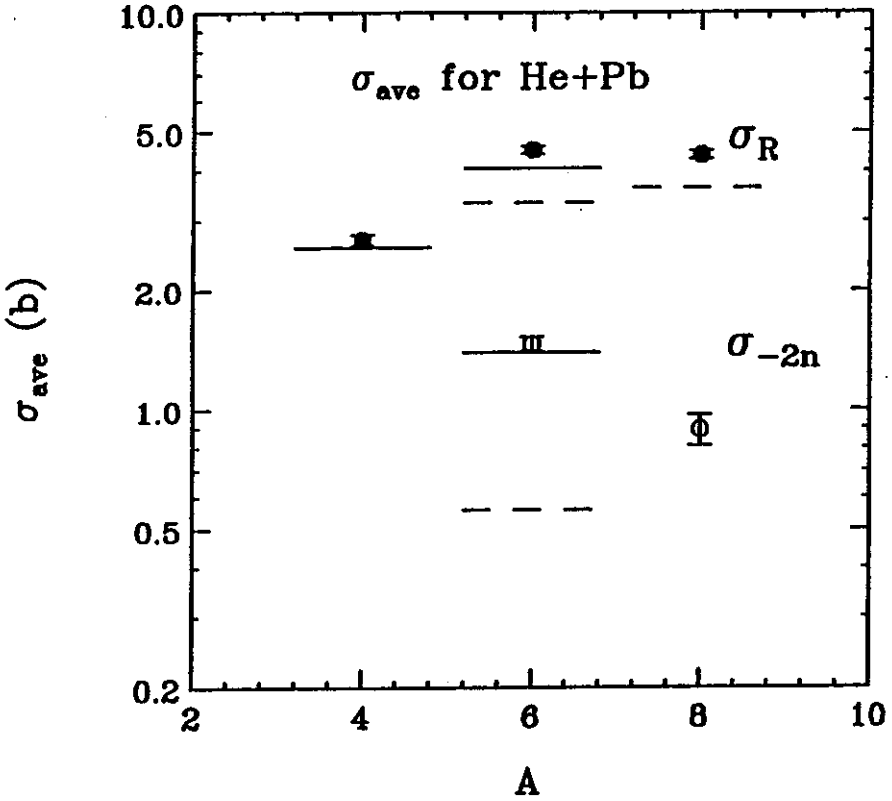
σ_{ave} for He+Pb
σ_R
σ_{-2n}
σ_{ave} (b)
A
10.0
5.0
2.0
1.0
0.5
0.2
2
4
6
8
10

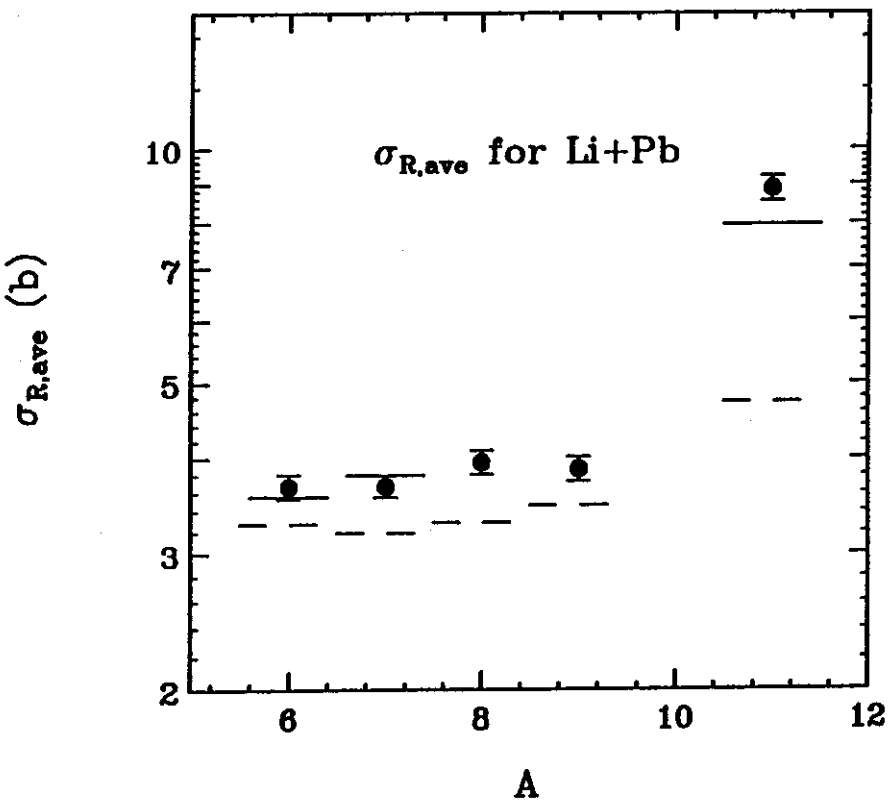
$\sigma_{R,ave}$ for Li+Pb
$\sigma_{R,ave}$ (b)
A
10
7
5
3
2
6
8
10
12

Warner

NEW Fig. 10